Additive Manufacturing 93 (2024) 104356

Contents lists available at ScienceDirect

Additive Manufacturing

journal homepage: www.elsevier.com/locate/addma

A novel solid-state metal additive manufacturing process – Laser-induced Supersonic Impact Printing (LISIP): Exploration of process capability

Yiliang Liao [a,*], Fazlay Rubbi [a], Bo Mao [b], Bin Li [a], Fatemeh Delzendehrooy [a], M. Merajul Haque [a]

[a] *Department of Industrial and Manufacturing Systems Engineering, Iowa State University, Ames, IA 50011, USA*
[b] *School of Materials Science and Engineering, Shanghai Jiao Tong University, Shanghai 200240, China*

ARTICLE INFO

Keywords:
Laser-induced supersonic impact printing
Solid-state metal additive manufacturing
3D micro-lamination of dissimilar metals

ABSTRACT

Solid-state metal additive manufacturing (AM) techniques offer unique capabilities for direct printing of metallic materials towards a variety of applications. In this work, we developed a novel solid-state metal AM process, named laser-induced supersonic impact printing (LISIP), in which the laser shock-induced impact loading was utilized to trigger the adiabatic shearing phenomenon at metal-metal interfaces towards solid-state three-dimensional (3D) printing of metallic materials. The design of LISIP was inspired by cold spray, explosive welding, and laser impact welding. An experimental investigation was conducted to explore the process capability of LISIP, with a focus on 3D micro-lamination of metallic structure, AM of dissimilar materials, and printing-on-demand direct writing at various length scales from micrometer to centimeter. Steel, copper, aluminum, titanium, and magnesium alloys were used as foil and/or substate for experimentation. Moreover, the microstructure at bonding interfaces were characterized to understand the microstructure evolution as induced by adiabatic shearing. The bonding quality was evaluated using the lap shear test. The mechanisms involved in LISIP including the laser-matter interaction and adiabatic shearing bonding were investigated using first-principles modeling and finite element method simulation. In addition, the technical challenges, scientific knowledge gaps, future research directions, and potential applications of LISIP were deliberated. We envision that the findings and knowledge gained in this work will serve as the first milestone towards the establishment of LISIP for broader impacts.

1. Introduction

Solid-state metal additive manufacturing (AM) techniques, particularly those operated under ambient conditions (such as ultrasonic AM [1–4], friction stir AM [5–8], and cold spray AM [9–13]), offer exceptional process capabilities for three-dimensional (3D) printing of metallic materials towards unique applications. As compared to high-temperature, fusion-based metal AM processes (laser powder bed fusion [14,15], direct energy deposition [16,17], electron beam melting [18], etc.), solid-state metal AM under ambient conditions does not require external thermal inputs during printing, leading to the avoidance of solidification and/or cooling-related defects (hot cracking, porosity, elemental loss and segregation etc.), the high compatibility and manufacturability when printing nonweldable materials, and the relatively homogeneous microstructure and properties. For instance, ultrasonic AM was successfully employed to print copper/aluminum (Cu/Al) laminated metal composites with a superior combination of strength and ductility [1]. Experimental investigations of friction stir AM demonstrated the process capability of fabricating Al alloys with homogeneously distributed microstructure due to the effect of continuous dynamic recrystallization during printing [7,8]. Moreover, the stainless steel and copper specimens fabricated using cold spray AM exhibited great mechanical properties (strength, ductility, and fatigue life) comparable to as-cast counterparts [11,12].

Despite aforementioned advancements, the development of novel strategies for solid-state metal AM under ambient conditions remains challenging, since the process innovation is often dependent on new material bonding mechanisms and/or creative process designs. Critical requirements for solid-state metal AM design include room-temperature operation with limited external thermal inputs, great bonding strength between printing layers, high compatibility with a wide range of metals and alloys, limited material waste and energy consumption, etc.

One of the most promising strategies that satisfies these requirements is the solid-state build-up of metallic structures through supersonic

* Corresponding author.
E-mail address: leonl@iastate.edu (Y. Liao).

https://doi.org/10.1016/j.addma.2024.104356
Received 2 March 2024; Received in revised form 19 July 2024; Accepted 11 August 2024
Available online 7 September 2024

impact bonding. As demonstrated by a few well-established manufacturing processes including cold spray [19–25] and explosive welding [26–29], the robust bonding at metallic particle/layer interfaces can be achieved by the ballistic impingement of metallic particles or foils under ambient processing conditions. Based on extensive experimental results, it is well evidenced that the supersonic impact bonding is realized when the deposit metallic material impacts the substrate at an impact velocity sufficiently high to trigger the onset of shear instability, large straining, and material jetting at the bonding interfaces. As reported in literature [22–24], both experimental and computational efforts on cold spray demonstrated that a critical particle velocity of ~500 m/s or higher was required for impact bonding, and a higher particle velocity led to a better bonding quality in terms of interface morphology and bonding strength. Previous investigations on explosive welding of Al alloys and stainless steels indicated that a high impact velocity of 400–600 m/s results in extremely large plastic strain of ~300 % at bonding interfaces and a materials jetting velocity up to 4000 m/s [26]. A recent experimental effort on explosive welding of Ti and steel reported that, different detonation wave zones with various impact velocities led to nearly straight, periodic wavy, or irregularly wavy interfaces, resulting in the tensile strength varying from 500 to 700 MPa in tensile testing with the bonding interface parallel to the tensile direction [27].

From the fundamental perspective, for the solid-state impact bonding mechanism, the supersonic impact velocity introduces a large interfacial strain as well as the disruption of oxide film as accompanied by the localized fragmentation and material jetting phenomena. As a result, a clean interfacial contact at the atomic level is achieved, leading to the formation of metallic bonds for material consolidation. Note that, besides the supersonic gas jet utilized in cold spray and the chemical detonation adopted in explosive welding, the metallic particles/foils could be accelerated to a supersonic velocity by nanosecond pulsed laser shock processing (LSP), such as laser impact welding [30–34] and high-velocity laser accelerated deposition [35]. In LSP, the laser-matter interaction leads to the evaporation and ionization of absorption materials and thus the generation of laser-induced high-energy plasma. While the hydrodynamic expansion of laser-induced plasma is confined by the transparent confinement, the localized plasma pressure is significantly increased to the level of several to tens of GPa, which has been extensively utilized for advanced manufacturing techniques, such as laser shock peening [36–38] and laser peen forming [39–41]. It is worth noting that the laser-induced plasma in LSP normally exhibits a plasma front velocity up to 10^3 m/s [42–46], which is ideal for promoting the material acceleration towards supersonic impact bonding. Previous investigations on laser impact welding have demonstrated the capability of LSP to impinge thin metallic foils onto metallic substrates for localized spot welding of a variety of metals and alloys, including stainless steels [47], Al alloys [33], titanium (Ti) alloys [31], etc. Moreover, LSP holds exceptional advantages including room-temperature and non-vacuum processing, high controllability of laser energy, and high geometric flexibility. Therefore, it is of tremendous interest to develop LSP-based AM strategy to realize solid-state 3D printing of metals and alloys under ambient conditions.

In this work, we developed a novel LSP-based AM process, named laser-induced supersonic impact printing (LISIP), in which the nanosecond laser shock-induced impact loading was utilized for solid-state 3D printing of metallic materials under ambient conditions. The process capability of LISIP was investigated, with a focus on multi-layer microscale AM, particularly 3D micro-lamination of dissimilar materials using steel, Cu, Al, Ti, and magnesium (Mg) thin foils. Moreover, the microstructure at bonding interfaces were characterized and the bonding quality was evaluated using tensile shear tests. The mechanisms involved in LISIP were discussed. In addition, the technical challenges, scientific knowledge gaps, future research directions, and potential applications of LISIP were deliberated. We envision that the findings and knowledge gained in this work will serve as the first milestone towards the establishment of LISIP for broader impacts.

2. Process concept and experimental details

From the process concept perspective, during LISIP printing, once the laser energy was absorbed by the ablative layer (used for absorbing the laser energy and protecting the metal surface from any laser-induced damage), the laser-induced plasma is formed. Since the hydrodynamic expansion of laser-induced plasma is confined by the transparent confinement, the localized laser-induced high-pressure shockwave is generated. Once the laser-induced shear stress during laser punching is greater than the shear strength of the metal foil, dynamic punching is triggered, leading to the launching of metal flyer with a supersonic flying velocity. If the impact velocity is sufficient high (critical velocity), the impinging between the metal flyer and previous printed layers or substrate results in the oxide layer removal, large straining, material jetting, and therefore solid-state bonding at the impinging interfaces.

Schematic illustrations of the LISIP system and experimental details are shown in Fig. 1. A Surelite III Nd-YAG laser (Continuum Inc.) with a wavelength of 1064 nm and a pulse duration of 7 ns was to deliver the laser energy (Fig. 1a). F-theta lens was applied to control the laser beam size. The LISIP printing stage was equipped with a computer-controlled multi-axis precision position system (a minimal step resolution of 0.002 in.). To set up the LISIP experiment (Fig. 1b), a graphite layer serving as the ablative layer (commercially available graphite lubricant from Asbury Carbons Inc.) was spray coated on the metal foil [48–50]. A transparent BK7 glass (McMaster-Carr) was applied as the confinement. A mechanical clamping system was used to tightly load the confinement, ablative layer, and metal foil, in order to optimize the laser-induced

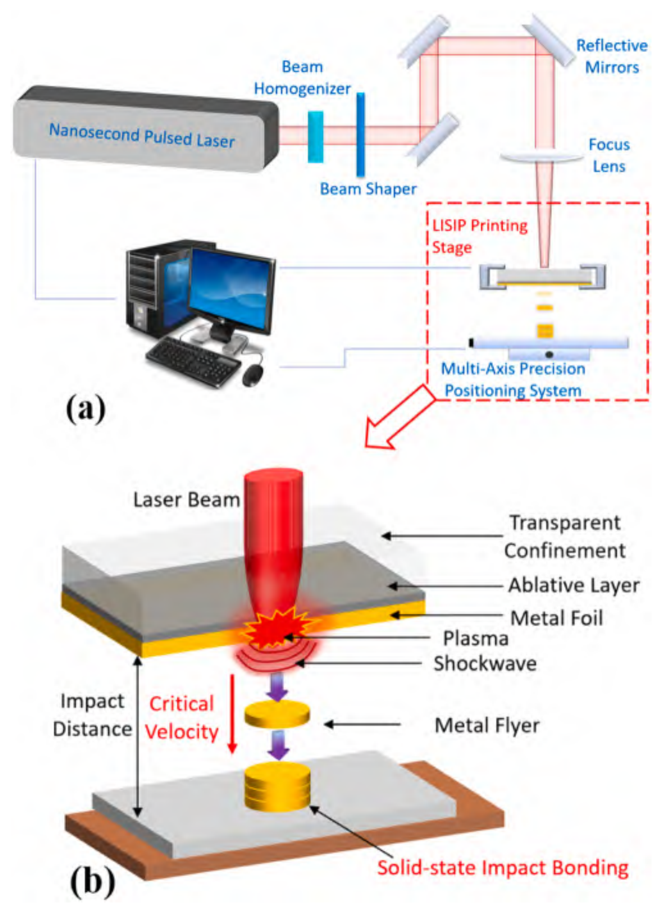

Fig. 1. Schematic illustrations of LISIP: (a) laboratory-scale LISIP system; and (b) details of experimental setup, laser-matter interaction, and solid-state impact bonding during LISIP.

shock pressure. In our experiments, the laser processing parameters included: laser intensity of 2–8 GW/cm^2, focused laser beam size of 1–2 mm in diameter, ablative layer of approximately 50 μm in thickness (as estimated), impact distance of 100 μm-500 μm, and the laser printing direction perpendicular to the substate surface (collision angle of 0°). The impact distance was selected and adjusted based on previous studies on laser impact welding [51–53]. A variety of metallic thin foils were used as feedstock materials for printing, including Al foils (10, 30 or 50 μm in thickness), Ti foil (50 μm in thickness), Cu foil (50 μm in thickness), and Fe foil (25 μm in thickness). Substrate materials include pure Al, 304 stainless steel, and AZ31B Mg alloy. Note that, if a more uniform energy distribution of laser beam is needed for precise manufacturing, a beam homogenizer can be integrated into the laser system as shown in Fig. 1a (we did not use beam homogenizer in this work, since Gaussian beam can achieve desired solid-state bonding). For multi-layer printing, the material was printed spot-by-spot, with the flyer material's position adjusted after each spot was printed using a X-Y table positioning system.

The microstructure evolution during LISIP was characterized using SM-7100FT field emission scanning electron microscope (FESEM), energy dispersive X-ray spectroscopy (EDS), and electron backscattered microscope (EBSD). In the preparation of samples for FESEM characterization, detailed processes including sectioning, mounting, polishing, and chemical etching were executed. EBSD analyses were carried out to study the crystallographic texture evolution. Samples subjected to EBSD analysis were vibrationally polished with a 0.06 μm diamond suspension

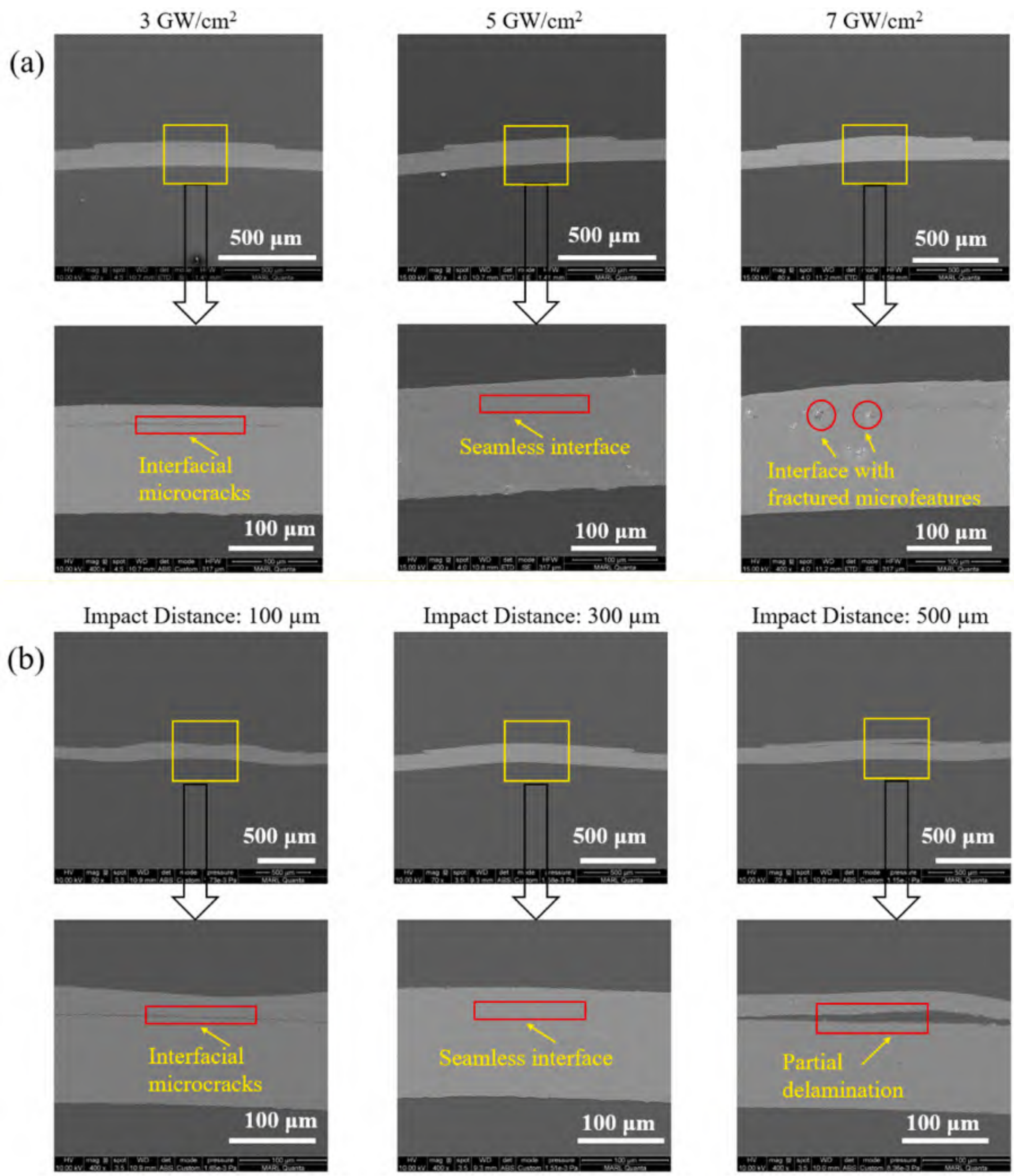

Fig. 2. (a) The effect of laser intensity on Al-Al interfaces: interfacial microcracks, seamless interface, and interface with fracture microfeatures of samples processing with laser intensity of 3, 5, and 7 GW/cm2, respectively (impact distance of 300 μm). (b) The effect of impact distance on Al-Al interfaces: interfacial microcracks, seamless interface, partial delamination of samples processed with 100, 300, and 500 μm, respectively (laser intensity of 5 GW/cm^2).

for 4 hours. The samples designated for EBSD analysis underwent vibrational polishing using a 0.06 μm diamond suspension for a duration of 4 hours, followed by etching. EBSD scans were conducted using HKL Channel 5 data acquisition software, covering an area of 200 μm by 200 μm with a precision step size of 0.5 μm. Samples for the tensile shear tests were prepared following the criteria outlined in the ASTM D3165 standard [54,55]. An Instron testing machine was used to control the tensile speed of 0.01 mm/s and record the load vs. displacement behavior. Tests were stopped as cracks initiated (indicated by a 10 % drop of the maximum load).

3. Experimental results

In this work, LISIP experiments were systematically conducted, aiming at evaluating the feasibility of the proposed novel AM strategy and demonstrating the process capability toward solid-state 3D printing of dissimilar metallic materials at different length scales.

3.1. Demonstration of LISIP process capability

3.1.1. 3D micro-lamination of metallic structure

LISIP experiments were carried out to fabricate 3D micro-laminated Al structure, using 30-μm-thick Al foil and pure Al substrate. Note that, Al alloy 7075 foils were used, which were normally considered as unweldable material [56]. Firstly, we studied the laser intensity effect on the bonding interface, as shown in Fig. 2a. Given a constant impact distance of 300 μm, the interface with microcracks, seamless interface, and interface with fracture microfeatures were clearly observed in samples processing with a laser intensity of 3, 5, and 7 GW/cm^2, respectively. Furthermore, the effect of impact distance was investigated. As shown in Fig. 2b, given a laser intensity of 5 GW/cm^2, the impact distance of 300 μm resulted in seamless bonding, while the impact distance of 100 or 500 μm led to the observable interfacial microcracks or partial delamination, respectively. Therefore, a laser intensity of 5.0 GW/cm^2 and an impact distance of 300 μm were selected for Al-Al printing.

Accordingly, single-layer and multi-layer LISIP experiments were successfully conducted, as shown in Fig. 3. The cross-sectional microstructure of single-layer printing was characterized by SEM and EBSD (Figs. 3a and 3b). It was found that a seamless foil-substrate interface was achieved, without any observable porosity, spatial gap, or microcrack. As observed in Fig. 3b, the seamless metallic bonding at interfaces was realized. Note that the SEM and EBSD images in Fig. 3b were taken from the same area of interface. Dynamic recrystallization of grains at interfaces is further discussed in Fig. 6. The similar results have been extensively reported in laser impact welding experiments [30–34]. More importantly, multi-layer LISIP of Al foils was performed to demonstrate the process capability of 3D micro-lamination of metallic structure. As shown in Figs. 3c and 3d, 6 layers of Al foils were printed with the build direction perpendicular to the substrate surface. From the SEM image and EDS analysis, the printing interfaces possessed different morphological features as the printing layer increased. In specific, the wavy interface was observed between the 1st and 2nd layer, while the smooth interface was identified between the 5th and 6th layer. With the increase of printing layer, the number of wrinkles at interfaces decreased gradually. Note that it is well accepted that the interface morphology of micro-laminated structures plays a critical role in determining their bonding strength and quality due to the mechanical locking effect. Similar to the fusion-based metal AM processes where the thermal cycle affects the microstructure of previous printed layers [14–18], the cyclic impact loading during LISIP is expected to introduce cyclic mechanical stress to previous printed layers, leading to the change of interface morphology. Moreover, it is also observed that the cyclic impact loadings during LISIP introduce cyclic compression to the previously printed layers, leading to the reduction of layer thickness as compared to the original thickness of printing foils. This interesting phenomenon requires further investigation to understand how the changes of interface morphology and layer thickness are affected by the cyclic impact

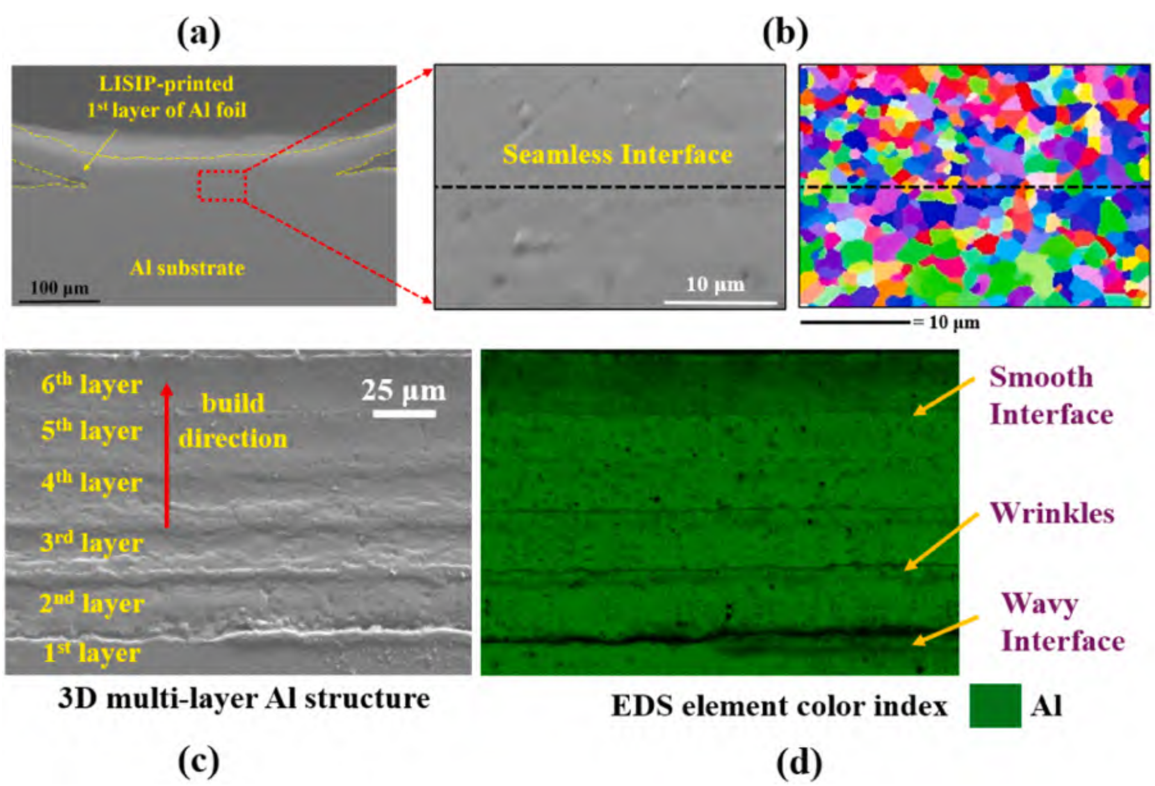

Fig. 3. 3D micro-lamination of Al structure using LISIP: (a) SEM and (b) SEM and EBSD images showing LISIP printing of single-layer Al thin foil on Al substrate with seamless interface; and (c) SEM image and (d) EDS analysis showing 3D micro-lamination of Al structure.

loading, and how the changes affect the bonding strength and quality of LISIP-fabricated metallic structure.

3.1.2. AM of dissimilar metallic materials

As compared to fusion-based metal AM processes, solid-state metal AM techniques often possess a major advantage of printing dissimilar materials, such as demonstrated by ultrasonic AM [1–4] and friction stir AM [5–8]. In this work, LISIP's capability of printing dissimilar materials was evaluated, as shown in Fig. 4. Given a laser intensity of 5 GW/cm^2, the Al foil with a thickness of 10 μm was bonded to the Mg substrate using LISIP. The SEM image in Fig. 4a showed a smooth morphology at the Al-Mg interface, and the EDS analysis in Fig. 4b indicated no obvious elemental diffusion during the ultrafast impinging of Al and Mg induced by laser shockwave. Furthermore, the steel-Cu-Al-Ti micro-laminated composite was successfully fabricated using LISIP (Figs. 4c-4e). Intuitively, we think various laser intensities should be applied to various materials. However, based on our experiments, we find that 5 GW/cm^2 is a good choice for those metal foils employed in this work. This is further validated by the lap shear testing results in Fig. 7. One possible explanation is that, during LISIP, the laser-induced supersonic velocity and ultrahigh impact loading (strain rate) are the dominant parameters for solid-state bonding, while the effect of intrinsic material properties is relatively limited (particularly considering the thin thickness and light weight of metallic foils). On the other hand, the laser-induced velocity and impact loading are mainly determined by laser intensity. Therefore, 5 GW/cm^2 works for those metallic foils used in our work. The OM and SEM images in Figs. 4c and 4d showed a smooth steel/Cu interface while a wave interface between Al and Ti layers. The similar wave Al-Ti interface was reported as the materials were bonding by laser impact welding [31]. It was found that the higher impact velocity led to waves of higher amplitude and shorter wavelength. The EDS analysis in Fig. 4e confirmed that no intermetallic compounds or third phase were generated at interfaces during LISIP. EDS line scan showed a sharp change of composition at bonding interfaces, where the 2-μm-width composition changing zone at interfaces was attributed to the EDS resolution. It is clearly observed that, LISIP exhibits exceptional capability of printing dissimilar materials due to the supersonic impact bonding mechanism (as discussed in Section 4).

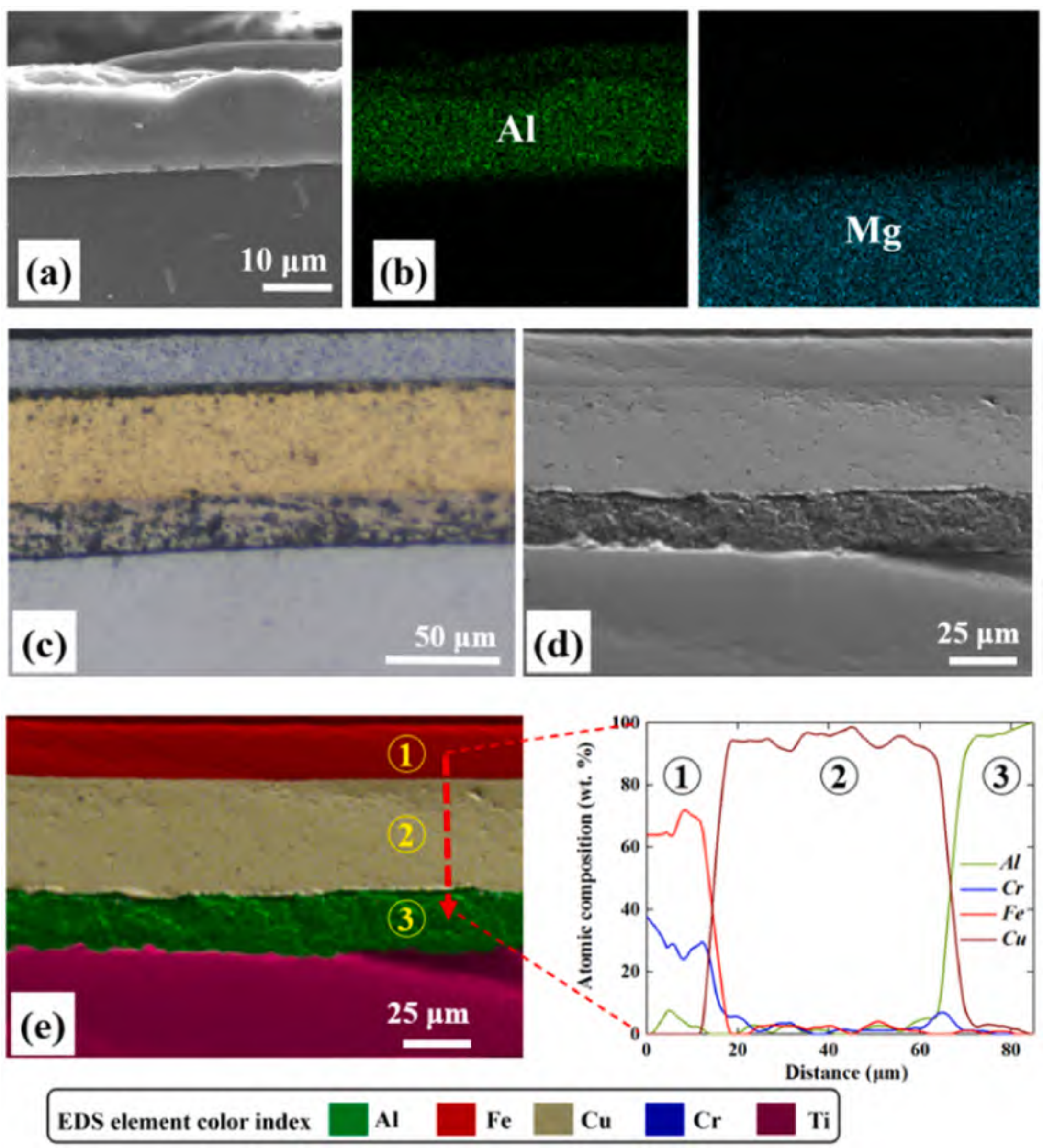

Fig. 4. AM of dissimilar materials using LISIP: (a) SEM image and (b) EDS analysis showing LISIP printing of Al on Mg substrate; and (c) OM image, (d) SEM image, and (e) EDS analysis showing LISIP-fabricated steel-Cu-Al-Ti micro-laminated composite.

3.1.3. Printing-on-demand solid-state direct writing

Direct metal printing or writing processes offer the capability of rapid, contact-free deposition of metallic materials towards applications in microelectromechanical systems (MEMS), micro-electronics, hierarchical materials, etc. Unlike the drop-on-demand (e.g. laser-induced forward transfer [57]) or solution-based (e.g. inkjet printing [58]) approaches, LISIP could be designed for solid-state direct metal writing without in-situ heating to form liquid metal micro-drops or post-printing thermal annealing. In this work, LISIP experiments were conducted to demonstrate the process capability of printing-on-demand solid-state direct metal writing. Given a laser intensity of 5.0 GW/cm^2 and laser beam size of 2 mm in diameter, 30-μm-thick Al foil was written on Cu substrate, where the computer-controlled multi-axis precision positioning system was applied for localized printing. The printing process was schematically illustrated in Fig. 5a, and the printing result was shown in Fig. 5b. As observed, Al spot pattern of "ISU" logo was successfully fabricated. SEM image in Fig. 5b showed the morphology of one printed Al spot, where the flat printing area was surrounded by a ring of material jetting zone. The SEM image with a high magnification and EDS analysis in Fig. 5c indicated the generation of localized fragmentations and shear bands in the material jetting zone due to large straining at the bonding interface. Considering the nature of solid-state printing, LISIP is expected to hold high compatibility with a wide range of metallic materials, particularly for those difficult-to-print metals using drop-on-demand strategies due to their high melting points. Note that the results shown in Fig. 5 align with those achievable through conventional laser impact welding (spot welding). More importantly, Fig. 5 highlights the LISIP system's ability to perform print-on-demand writing in both the x and y directions. On the other hand, Figs. 3 and 4 demonstrate LISIP's capability to print multi-layers in the z direction. Taken together (Figs. 3–5), the prototype LISIP system excels in solid-state printing across all three dimensions towards AM of metallic structures.

3.2. Microstructure evolution at printing interfaces

Conceivably, the high impact velocity in LISIP might cause a conspicuous change in grain structure and texture in the materials near the interface. In cold spray, adiabatic shearing was reported as a result of high strain rate deformation. Adiabatic shear bands were typically observed in materials with a relatively low thermal conductivity and a low work hardening coefficient [19–25]. During impact loading, large plastic flow is incurred at a high strain rate. During dynamic deformation, the majority of the plastic work is converted to thermal energy which is unable to be dissipated to the surrounding material. As a result of the heavy plastic deformation and localized heating, dynamic recrystallization may occur. This behavior is indeed observed in our LISIP processing. Figs. 6a-6d showed the microstructure and texture evolution when Al foil was bonded to an Al substrate. Before LISIP (Fig. 6a), large grains can be observed in the Al foil. A strong {100} texture can also be seen. After LISIP (Fig. 6b), the grain size was significantly refined. The average grain size was reduced from 13 to 15 μm before printing to 4–6 μm after printing. Fine, new grains were formed as a result of dynamic recrystallization. The {100} texture was also weakened. Figs. 6c-6d showed the grain boundary distribution in the Al foil before and after LISIP. We highlighted the high angle grain boundaries (HAGBs) with a misorientation angle greater than 15° with black lines, whereas those low angle grain boundaries (LAGBs) were displayed as green lines. Again, a conspicuous grain refining can be observed during LISIP.

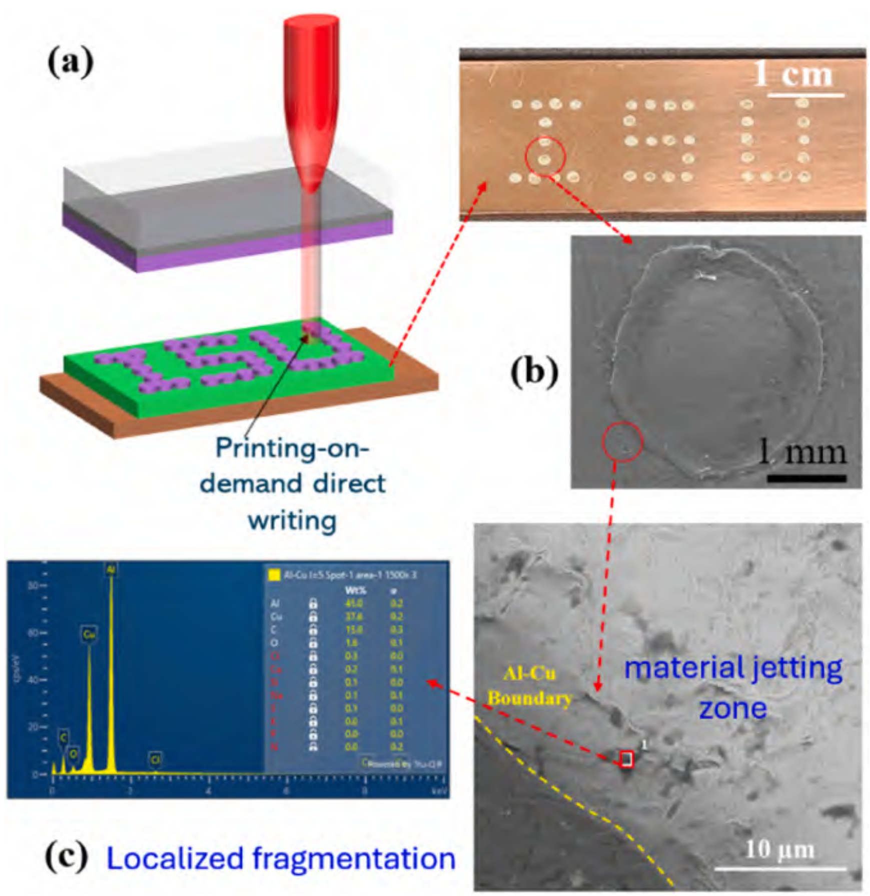

Fig. 5. Printing-on-demand solid-state direct writing using LISIP: (a) schematic illustration and (b) optical and SEM images showing direct writing of Al spot pattern of ISU logo on Cu substrate. (c) SEM image and EDS analysis showing one LISIP-printed Al spot with material jetting zone and localized fragmentation.

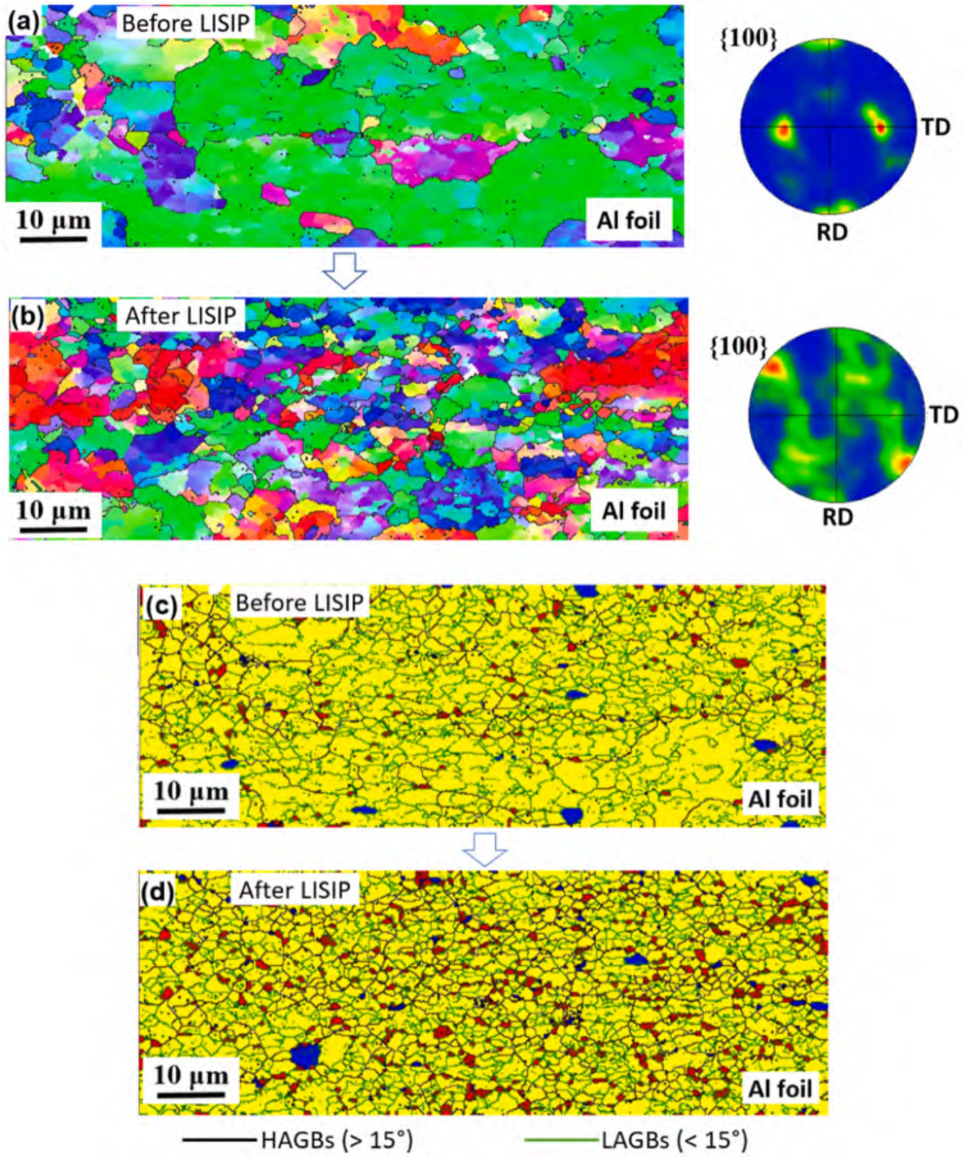

Fig. 6. Microstructure evolution at the printing interfaces in LISIP: (a) The grain structure and texture of the Al foil before LISIP. (b) Grain refining occurred during LISIP. After processing, the {100} pole figure indicated a weakened texture. (c) and (d) Grain boundary distributions before and after LISIP. The high angle grain boundaries (HAGB) with misorientation angle $> 15^{\circ}$ are highlighted with the black lines. Significant grain refining can be seen.

3.3. Evaluation of interfacial bonding strength

In order to evaluate the quality of LISIP-fabricated bonding interfaces, lap shear tests based on the ASTM D3165 standard [54,55] were conducted (as illustrated in Fig. 7a). Note that, the lap shear test has been extensively used to study the bonding quality for other sheet lamination processes. The fracture morphology of a LISIP-fabricated Al-Al joint after lap shear test was shown in Fig. 7b. As observed, the fracture occurred outside the bonding area while the bonding area remained intact, demonstrating the fracture mode of nugget pull-out (fracture of base material) rather than interface debonding. This fracture morphology and mode indicated a high-quality bonding interface was achieved by LISIP. The values of the failure loads at the fracture initiation as affected by the laser power intensity were summarized in Fig. 7c (the cases of Al-Al, Al-Cu, and Al-Ni joints). It was found that for all three cases, solid-state bonding can be achieved while the applied laser intensity was higher than 3.0 GW/cm^2, while the optimized bonding strengths were obtained by a laser power input of 5.0 GW/cm^2. For instance, of Al-Al joints, the optimized failure load was measured to be around 28 N, indicating a lap shear strength up to 18 MPa (defined as the ratio of loading force to bonding area). The recorded failure load was comparable to those of joints fabricated by laser impact welding as reported in literature, such as the failure loads of 18 N for Al/brass joints [59], 24 N for Al/Ti bonding [31], and 20 N for Cu/Al interfaces [60]. Moreover, the failure loads at various layer interfaces were measured using LISIP-fabricated multilayer Al structure. As observed in Fig. 7d, the increasing of printing layer does not have a significant effect on the interfacial bonding strength.

4. Discussion

In addition to experimental investigation, to gain a fundamental understanding of the process mechanism involved in LISIP, first-principles modeling of laser-matter interactions and finite element method (FEM) simulation of supersonic impact bonding were performed, aiming to understand the laser-induced shockwave propagation, the acceleration of metal flyer, and the large straining at the bonding interface.

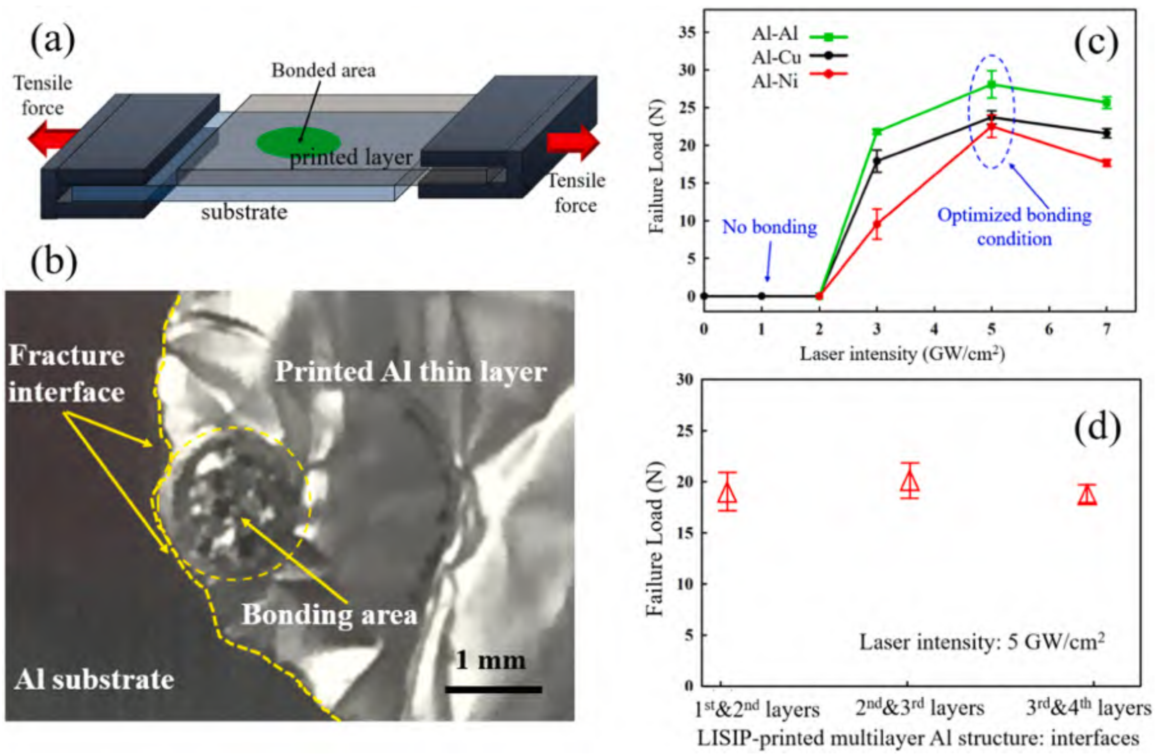

Fig. 7. Results of lap shear tests: (a) schematic of lap shear test; (b) fracture morphology indicating the fracture mode of nugget pull-out of LISIP-fabricated Al-Al joints; (c) failure loads as affected by laser intensity: the cases of Al-Al, Al-Cu, and Al-Ni joints; and (d) failure loads at various layer interfaces (the case of LISIP-fabricated multilayer Al structure).

4.1. Laser-Matter Interaction during LISIP

Comprehension of the governing mechanism in the LISIP process starts with the understanding of laser-matter interactions and the resulting plasma dynamics responsible for the acceleration of metal flyer. The comprehensive laser-matter interactions during LISIP can be considered as two steps: 1) absorption and conduction of laser energy; and 2) generation and expansion of laser-induced plasma.

In the first step of laser-matter interactions, once the nanosecond laser pulse interacts with the ablative material, the incident photon energy is rapidly absorbed by electrons, resulting in their instantaneous thermalization within femtoseconds. The subsequent electron-phonon emission leads to the energy transfer to the lattice at the time scale of picoseconds. The conservation of energy can be referred to [61,62]. The source term for the incident laser pulse is a function of laser intensity, the absorption coefficient and laser beam spot size. For a nanosecond laser pulse during LISIP, electrons and ions rapidly achieve thermal equilibrium for adequately long laser pulse. In the second step, during LISIP, the laser-induced plasma is generated by the cascade process of ionization, and the evolution of plasma is governed by the coupled mass, momentum and energy transport (MMET) processes. The plasma evolution can be described using a two-fluid MMET model, in which the plasma density, pressure, and plasma front velocity are quantified [61].

In our previous work [63], a first-principles theoretical model capable of predicting the plasma dynamics during nanosecond LSP was developed. Details of model development can be referred to [63], the modeling results were validated by reported experimental data. In this work, the LSP model was applied to simulate the temporal evolution of laser-induced plasma pressure in LISIP. The predicted pressure profile was used as an input for FEM simulation of laser-induced impact bonding mechanism. As illustrated in Fig. 8, given a laser wavelength of 1064 nm and laser pulse duration of 7 ns, the peak pressure of laser-induced plasma increases from 4.6 to 5.8 GPa by increasing the laser power intensity from 5.1 to 6.4 GW/cm^2. A sharp increase of plasma pressure is observed until 20 ns, followed by a gradual decrease over time. The pressure profile lasts longer than 100 ns, providing sufficient duration for launching and accelerating the metal flyer during LISP.

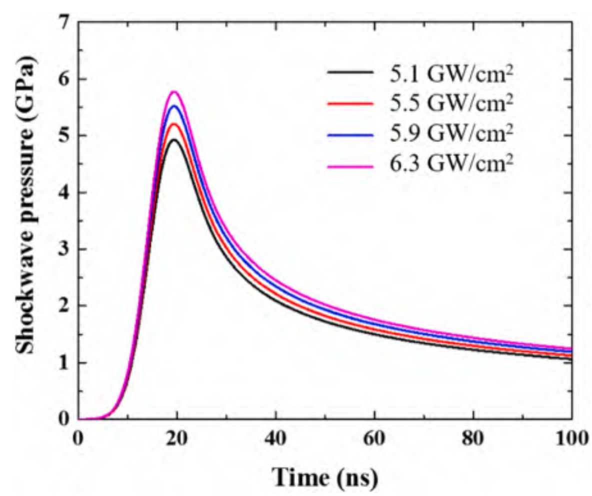

Fig. 8. The simulated temporal evolution of laser-induced shockwave pressure during LISIP.

4.2. Solid-state impact bonding during LISIP

Aiming to advance the understanding of metal flyer acceleration and solid-state interlayer impact bonding during LISIP, a two-stage computational 3D FEM model was developed using ABAQUS software. Considering the high-velocity impact and significant deformation during LISIP, a dynamic explicit method was employed [64–69]. Figs. 9a and 9b

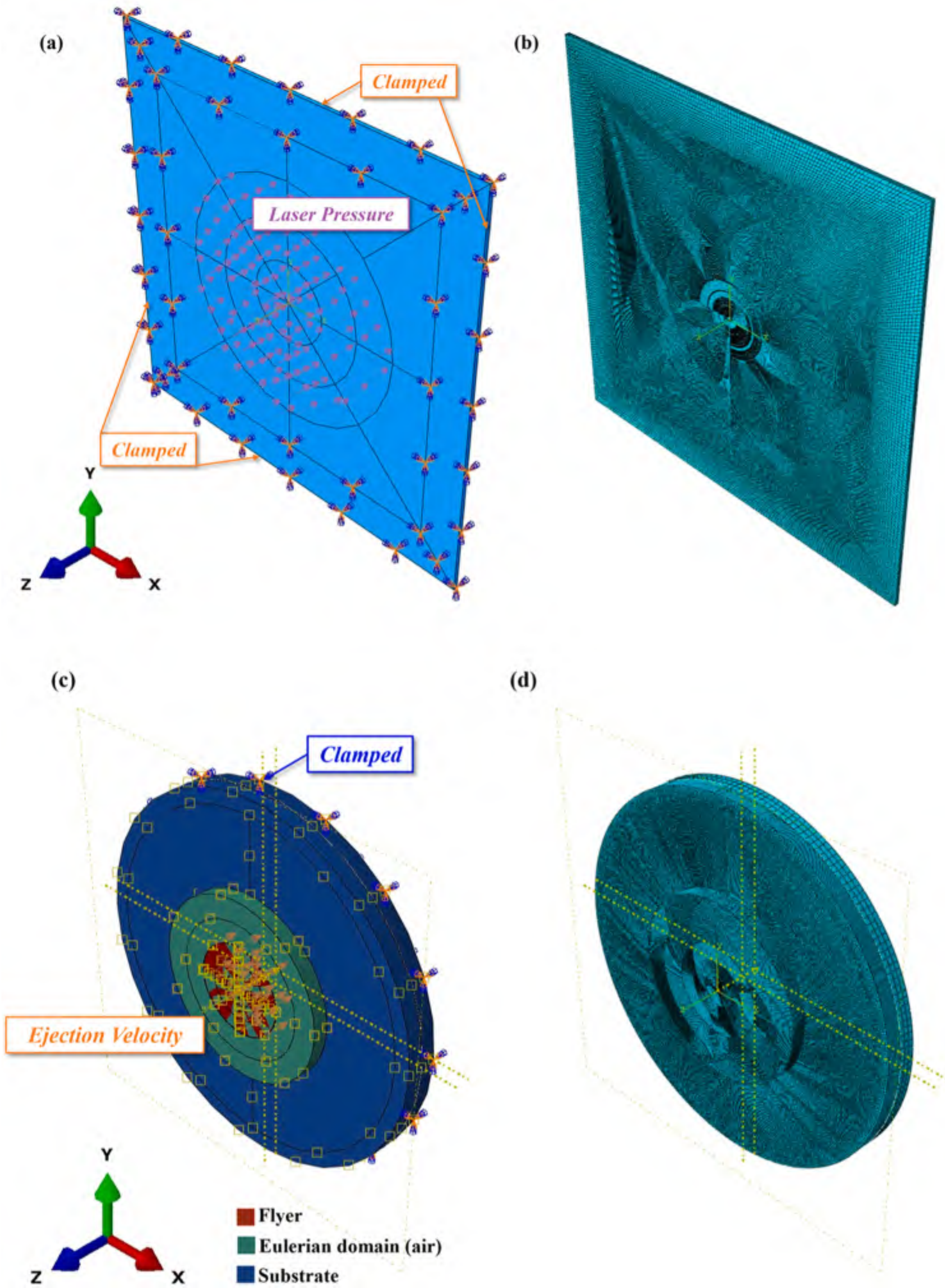

Fig. 9. FEM model to simulate laser-induced acceleration of metal flyers in LISIP: (a) loading and boundary conditions in a fully Lagrangian model, and (b) FEM mesh. FEM model to simulate supersonic impact bonding in LISIP: (c) loading and boundary conditions for the coupled Eulerian-Lagrangian model, and (d) FEM mesh.

showed the model configuration for simulating the laser-induced acceleration of metal flyer (Stage I), where the predicted temporal evolution of laser shock pressure in Section 4.1 was uniformly applied across a circular area as the mechanical loading input, and the size of circular area was defined by the laser beam diameter. Lagranigain's numerical approach was employed [64], and the C3D8RT elements were assigned to the thin foil with hourglass control. The front and rear corners of the thin foils were clamped to simulate the experimental condition.

The focus of simulation effort in Stage II was placed on understanding the adiabatic sharing mechanism in terms of interfacial large straining, material jetting, and localized temperature profile. To simulate Stage II, the Eulerian approach [70] was applied to model the scenario of extreme deformation during solid-state impact bonding, since it sidesteps the limitation of mesh distortion inherent to traditional Lagrangian approach. The Coupled Eulerian-Lagrangian (CEL) analysis [64–66,68] was employed, allowing materials in the Eulerian domain to interact with elements in the Lagrangian domain via Eulerian-Lagrangian contact. Figs. 9c and 9d showed the model configuration for Stage II, where the dimensions of metal flyer were set to 1.5 mm in diameter and 30 μm in thickness, the substrate was considered as a cylindrical solid (3 mm in diameter and 500 μm in thickness) with the backside being completely fixed, and an impact distance of 300 μm was applied. As reported in literature focusing on cold spray modeling [64–67], to address the mesh sensitivity issue, it was recommended to use a mesh size as 1/25 of the radius of impinging particles in cold spray. In this study, the mesh size in the impact bonding zone was set as 1/25 of the thickness of metal flyer. The flyer and substrate were meshed by C3D8RT element, whereas the Eulerian domain was simulated using EC3D8RT element. An advanced Eulerian-Lagrangian contact formulation based on an enhanced immersed boundary method was applied [64–66,68]. To simulate the elastic, plastic, and damage behaviors of the material, the Mile--Grüneisen equation [71], the Johnson-Cook model [72,73], and the Johnson-Cook ductile damage criteria [72,73] were employed, correspondingly. Detailed equations can be referred in [71–73].

In this study, LISIP modeling was performed to investigate laser-induced Al to Al bonding. Simulation parameters include the laser intensity of 5 GW/cm^2, beam size of 1.5 mm, corresponding peak pressure of 4.7 GPa, and simulation duration of 200 ns for both Stage I and Stage II. Other material properties and parameters were summarized in Table 1 [52,64]. The FEM modeling results of Stage I were presented in Fig. 10. As observed in Figs. 10a and 10b, a dramatic increase of velocity was induced at the beginning of the process until 30 ns, when the shockwave pressure reached its maximal value. Afterwards, while the shockwave pressure was alleviated, the rate of escalation in velocity slightly decreased. As the processing time reached 60 ns, the velocity approached a plateau with slight fluctuation around 1250 m/s, since the damage initiation at this point and the shockwave energy is dissipated by damage propagation. As shown in Fig. 10c, the maximal von-Mises stress higher than material's ultimate tensile strength occurred at the circumference of laser beam area, resulting in the damage initiation sites (80 ns). As time passed, at 120 ns, the partial separation of the flyer from the metal foil was observed. Once time reaches 160 ns, the flyer was fully separated from metal foil and projected with a projection velocity of 1250 m/s. Note that the simulated metal flyer velocity is comparable to the measured experimental data in literature of laser impact welding. It was reported that given a Al foil with a thickness of 25 μm, the measured impact velocity is as high as 1000 m/s, and the impact velocity decreased with the increase of metal flyer thickness [31].

Using the impact velocity of 1250 m/s, FEM simulation of Stage II was conducted. Fig. 11 depicted the temporal evolution of equivalent plastic strain, shear stress, temperature, and the resultant velocity vectors at the bonding interfaces. As shown in Fig. 11, the initiation of material jetting phenomena was observed at 10 ns, where an intense plastic strain (~200 % in Fig. 11a) occurred at the boundary of the flyer, and the resultant velocity vectors were highly directed outwards at the flyer boundaries (Fig. 11d). The supersonic impact loading resulted in a localized concentration of interfacial deformation particularly at the edges of the flyer, which was where the material experienced the most intense shear. The localized plastic strain increased over time with an average strain level of 300 % in the material jetting zone at 40 ns (Fig. 11a). Meanwhile, as predicted in Fig. 11b, the compressive stresses at the bonding interface and material jetting zone with a value as high as −280 MPa occurred at the beginning of impact bonding until 10 ns. With the increase of loading time, the material spring back and jetting phenomena resulted in a redistribution of LISIP-induced compressive stress, where the compression zone with a deeper depth and a lower average stress value was generated. For instance, at 40 ns, the depth of compressive zone increased to larger than 100 μm and the average stress level was reduced to −40 MPa. The combined frictional heating, shearing motion and high-pressure contact conditions generates heat at interface and results in temperature elevation at the boundaries of the flyer and the substrate. These high strain shearing and high-pressure contact at the bonding interfaces led to a substantial thermal response upon contact. As predicted in Fig. 11c, the interface temperature rapidly escalated up to ~600 K at the beginning of impact bonding, indicating a highly exothermic interface phenomenon. The instantaneous temperature elevation at interface might cause thermal softening, benefiting the interfacial straining. At 10 ns, a discernible thermal diffusion was observed with the heat propagating into the substrate. A pronounced temperature gradient remained concentrated around the flyer periphery. In fact, these phenomena occurred in a short duration with inadequate time for heat dissipation. This was well accepted as the adiabatic shearing mechanism. Moreover, the velocity vector field predicted in Fig. 11d showed that the high relative motion at bonding interfaces increased over time and reached ~700 m/s at 40 ns at the flyer edge, indicating the pronounced material jetting behavior as a result of adiabatic shearing.

Table 1
Material parameters of Al used for FEM simulation of LISIP [57,67].

Mass Density, ρ (kg/m^3)	2710	c_0 (m/s)	5380
Shear Modulus, G (GPa)	27	s	1.337
Heat Conductivity, k (W/mk)	273.2	Γ_0	2.1
Specific Heat, c (J/kgK)	898.2	T_0 (K)	273.2
A (MPa)	148.4	T_m (K)	916
B(MPa)	345.5	D_1	0.5
n	0.183	D_2	4.89
m	0.895	D_3	3.03
C	0.025	D_4	0.014
$\dot{\varepsilon}_0$	1	D_5	1.12
Friction Coefficient, μ	0.3		

4.3. Engineering challenges and future research directions

Despite experimental data and modeling results in this study, as an innovative solid-state metal AM process, LISIP is still in its infant stage, and further investigations are required to fill scientific knowledge gaps and tackle engineering challenges towards the establishment of LISIP for a variety of industrial applications. The potential challenges and proposed future research directions are discussed as following:

- Understanding of process-microstructure relationships. Future experimental efforts are expected to focus on investigating the process-microstructure relationship during LISIP. Detailed correlations between processing conditions (laser intensity, beam size, metal foil thickness, impact distance, impact angle, etc.) and microstructural features (interfacial morphology, grain size, void, dislocation/twinning density, etc.) need to be developed for process control and optimization. To achieve this objective, a scientific understanding of interfacial dynamic recrystallization as affected by adiabatic shearing is of specific importance. Moreover, similar to the cyclic thermal loading during fusion-based metal AM, particular attention should be placed on the cyclic impact loading effect on the interfacial microstructure evolution.
- Elucidation of laser-induced solid-state bonding mechanism. It is well accepted the supersonic impact bonding is accompanied by adiabatic shearing phenomena, where the oxide layer removal, large straining, materials jetting, and localized temperature rise take place at the bonding interfaces. However, it remains elusive if the metallic bonding at the atomic level is attributed to the interfacial diffusion mechanism. If so, how the atomic diffusivity is affected by intrinsic material properties (lattice structure, grain characteristics, strength-ductility synergy, etc.) and how the diffusion ratio is influenced by the LISIP conditions (impact velocity, impact angle, etc.). Fundamental investigations on the bonding mechanism during LISIP, particularly materials modeling and/or high-resolution microscopic imaging at the atomic level, are necessary for a complete understanding of process mechanism.
- Understanding of microstructure-property relationship. Understanding of properties of LISIP-printed structures as affected by microstructural features requires further research and development efforts. Particular attention is expected to be paid to investigate the effects of interfacial microstructure (grain structure and morphological features) on the mechanical performance of 3D-printed parts (strength, ductility, fatigue life, etc.). It is of specific interest to understand the effect of periodic laminated grain structure (coarse-refined-coarse-refined grains) on the strength-ductility synergy, and the effect of laser-induced compressive residual stresses on the

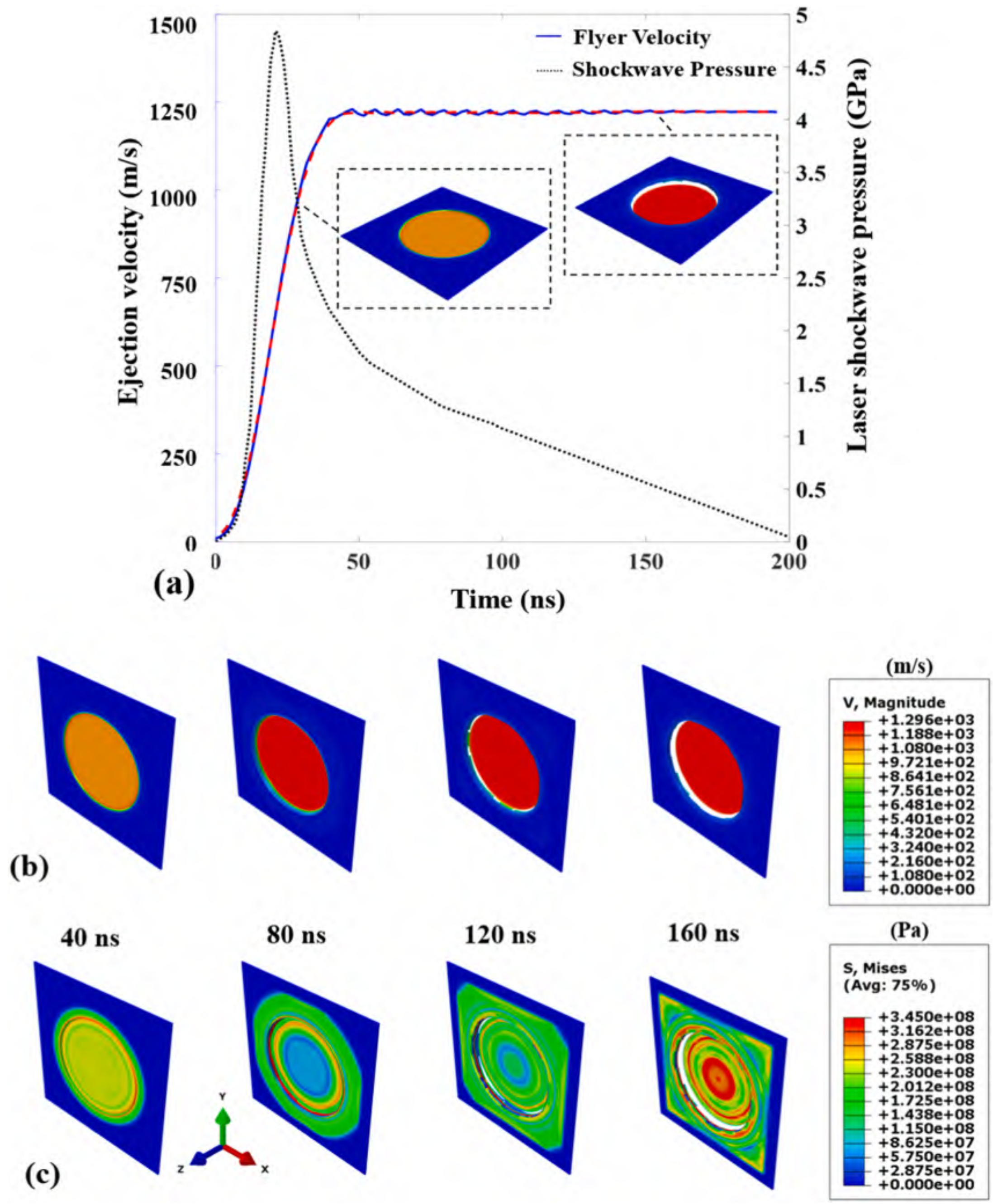

Fig. 10. FEM simulation of laser-induced acceleration of metal flyer during LISIP: (a) temporal evolution of flyer velocity and laser shock pressure; (b) contour plots of velocity; and (c) von Mises stress distribution.

improved material durability. We envision the gained knowledge will lead to future 3D geometric design of high-performance metals or alloys with multi-mode grain structures.

- Process scalability and macro-scale AM. The laboratory-scale LISIP system developed in our research has demonstrated the capability of LISIP for AM at the length scale from micrometer to centimeter. To enable macro-scale AM in industrial production systems, the industry-scale LISIP system needs to be developed, where a nano-second pulsed laser with a higher laser power is expected. Given the same level of laser intensity which is sufficient high to trigger the laser-induced solid-state bonding, the laser system delivering a higher laser power can be used for LISIP with a larger beam size, which is the critical bottleneck restricting the process scalability. In addition, further experimental study using a high-power laser system is needed to investigate the maximal metal foil thickness for LISIP, which is also beneficial for process scalability. However, utilizing a high-power laser system often leads to safety concerns and specific operation regulations, which need to be fully incorporated while developing the industry-level LISIP system.
- Process effectiveness and efficiency for AM of parts with complex 3D geometry. The same as other sheet lamination processes, post-printing machining is often required for achieving the pre-designed complex 3D geometry. We envision that industry-scale LISIP equipment should be integrated with a multi-axis machining tool to develop a hybrid manufacturing system (additive and subtractive manufacturing). This design concept has been realized for the commercialized industry-scale ultrasonic AM system. Moreover, to improve the process efficiency, a continuous metal foil delivery

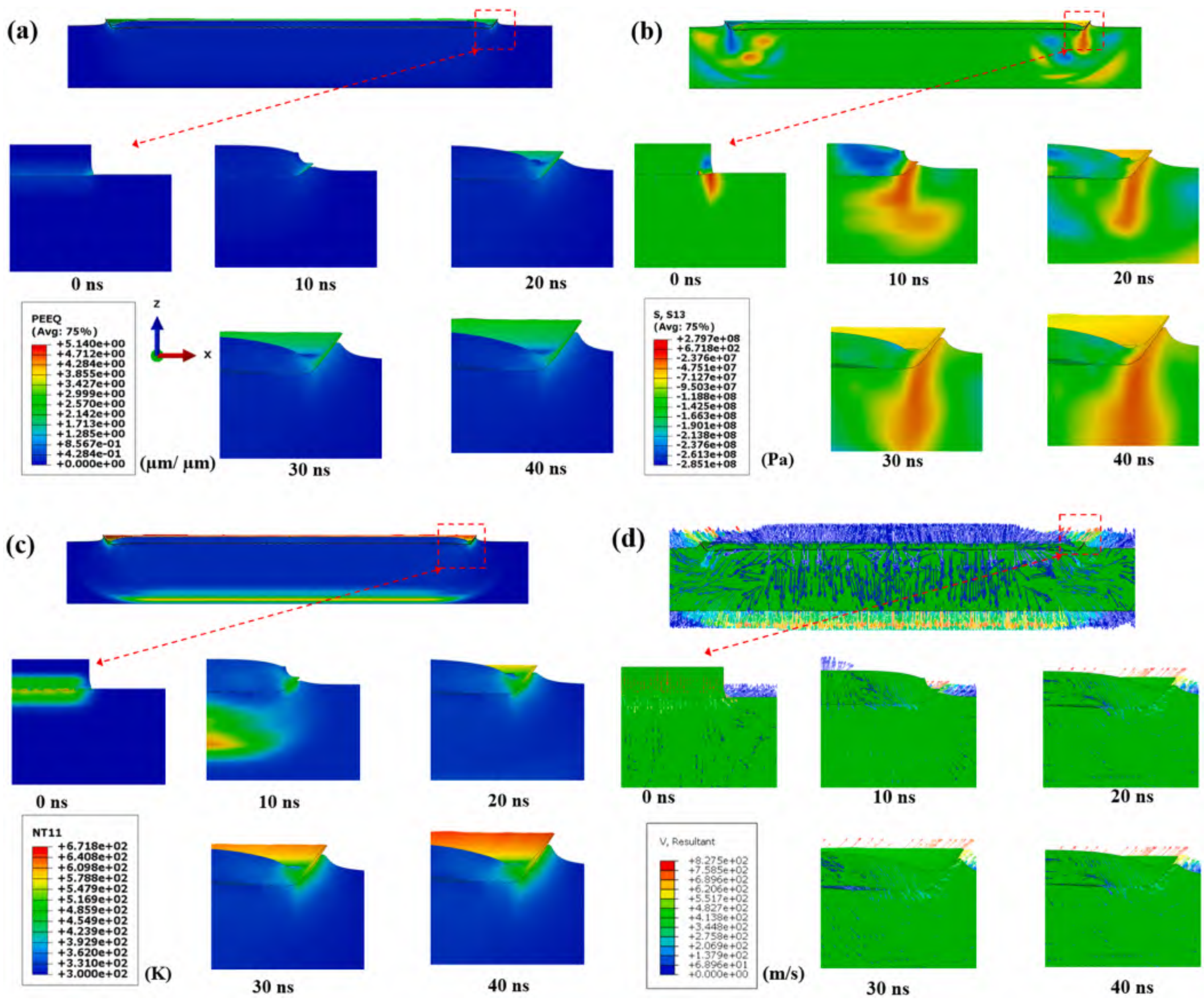

Fig. 11. FEM simulation of Al-Al impact bonding during LISIP: temporal evolutions of a) equivalent plastic strain, b) shear stress distribution, (c) temperature profile, and d) velocity vector field at the bonding interface.

system will be incorporated, such as utilized in roll-to-roll printing systems.

- Process applications. The success of LISP development is expected to find applications in various industries. LISIP-enable solid-state direct metal printing in micrometer or millimeter will benefit the designs of microelectromechanical systems (MEMS), micro-electronics, metamaterials, and hierarchical materials, such as AM of high-performance metal interconnects, contacts, and electrodes for flexible electronic devices, particularly for those requiring vertically stacked metal electrodes (thin-film transistors). In addition, LISIP's capability of printing dissimilar materials will lead to novel composite material designs with unique mechanical and/or physical properties towards structural, biomedical, or aerospace applications. The nature of solid-state bonding by LISIP will benefit the repair and remanufacturing of difficult-to-weld metallic materials such as Mg alloys.

5. Conclusions

In this work, a novel solid-state metal AM process, LISIP, was developed, in which solid-state 3D printing of metallic materials was realized by laser shock-induced impact loading. LISIP experiments were performed using a laboratory-scale LISIP system to evaluate the process capability. The interfacial microstructure was characterized, and the lap shear strength at bonding interfaces was tested. The process mechanisms were investigated by first-principles modeling of laser-matter interactions and FEM simulations of adiabatic shearing at metallic interfaces. The major conclusions include:

- Experimental data demonstrated LISIP's capability of achieving 3D micro-lamination of metallic structure, AM of dissimilar materials, and printing-on-demand direct writing at various length scales from micrometer to centimeter.
- High impact velocity at bonding interfaces during LISIP resulted in a significant grain refinement effect by dynamic recrystallization. The cyclic impact loading led to the change of interfacial morphology from smooth to wave interfaces.
- The lap shear test of LISIP-fabricated Al-Al joints showed a failure load up to 30 N, indicating a high-quality metallic bonding at Al-Al interfaces with a lap shear strength up to 18 MPa.
- The modeling results indicated that laser-induced shockwave during LISIP led to the impact velocity of metal flyer higher than 1000 m/s, the large plastic strain of over 200 % and the localized temperature

rise to 500 K at the bonding interfaces due to the adiabatic shearing mechanism.

Moreover, the scientific knowledge gaps and engineering challenges towards the establishment of LISIP were discussed, and the future research direction were proposed. We envision that the findings and knowledge gained in this work will serve as the very first milestone towards broad impacts of LISIP for various industrial applications.

CRediT authorship contribution statement

M. Merajul Haque: Investigation, Methodology. **Fatemeh Delzendehrooy:** Methodology, Investigation. **Fazlay Rubbi:** Investigation. **Bo Mao:** Methodology, Investigation. **Bin Li:** Writing – review & editing, Conceptualization. **Yiliang Liao:** Writing – review & editing, Writing – original draft, Supervision, Project administration, Investigation, Funding acquisition, Conceptualization.

Declaration of Competing Interest

The authors declare that they have no known competing financial interests or personal relationships that could have appeared to influence the work reported in this paper.

Data Availability

Data will be made available on request.

Acknowledgments

Y. Liao and B. Li gratefully thank the support from Iowa State University (faculty startup funding). B. Mao acknowledgments the funding support from the National Natural Science Foundation of China (No. 52101046).

References

[1] Y.Y. Zhou, F.C. Jiang, Z.Q. Wang, J.Y. Chen, Microstructure characteristics and mechanical properties of Cu/Al laminated metal composites fabricated by electropulsing assisted ultrasonic additive manufacturing, J. Mater. Process Tech. 313 (2023).
[2] V.K. Nadimpalli, G.M. Karthik, G.D. Janakiram, P.B. Nagy, Monitoring and repair of defects in ultrasonic additive manufacturing, Int. J. Adv. Manuf. Tech. 108 (5-6) (2020) 1793–1810.
[3] D.Z. Li, A review of microstructure evolution during ultrasonic additive manufacturing, Int. J. Adv. Manuf. Tech. 113 (1-2) (2021) 1–19.
[4] H.C. Hyer, D.C. Sweeney, C.M. Petrie, Functional fiber-optic sensors embedded in stainless steel components using ultrasonic additive manufacturing for distributed temperature and strain measurements, Addit. Manuf. 52 (2022).
[5] R.S. Mishra, R.S. Haridas, P. Agrawal, Friction stir-based additive manufacturing, Sci. Technol. Weld. Joi 27 (3) (2022) 141–165.
[6] A.K. Srivastava, N. Kumar, A.R. Dixit, Friction stir additive manufacturing - an innovative tool to enhance mechanical and microstructural properties, Mater. Sci. Eng. B-Adv. 263 (2021).
[7] R.J. Griffiths, D. Garcia, J. Song, V.K. Vasudevan, M.A. Steiner, W. Cai, H.Z. Yu, Solid-state additive manufacturing of aluminum and copper using additive friction stir deposition: process-microstructure linkages, Materialia 15 (2021).
[8] T. Jiang, T. Jiao, G.Q. Dai, Z.K. Shen, Y.H. Guo, Z.G. Sun, W.Y. Li, Microstructure evolution and mechanical properties of 2060 Al-Li alloy via friction stir additive manufacturing, J. Alloy Compd. 935 (2023).
[9] R. Melentiev, N. Yu, G. Lubineau, Polymer metallization via cold spray additive manufacturing: a review of process control, coating qualities, and prospective applications, Addit. Manuf. 48 (2021).
[10] G. Prashar, H. Vasudev, A comprehensive review on sustainable cold spray additive manufacturing: State of the art, challenges and future challenges, J. Clean. Prod. 310 (2021).
[11] S. Bagherifard, J. Kondas, S. Monti, J. Cizek, F. Perego, O. Kovarik, F. Lukac, F. Gaertner, M. Guagliano, Tailoring cold spray additive manufacturing of steel 316 L for static and cyclic load-bearing applications, Mater. Des. 203 (2021).
[12] C.Y. Chen, Y.C. Xie, S. Yin, W.Y. Li, X.T. Luo, X.L. Xie, R.X. Zhao, C.M. Deng, J. Wang, H.L. Liao, M. Liu, Z.M. Ren, Ductile and high strength Cu fabricated by solid-state cold spray additive manufacturing, J. Mater. Sci. Technol. 134 (2023) 234–243.
[13] R.F. Vaz, A. Garfias, V. Albaladejo, J. Sanchez, I.G. Cano, A review of advances in cold spray additive manufacturing, Coatings 13 (2) (2023).
[14] J.P. Oliveira, A.D. LaLonde, J. Ma, Processing parameters in laser powder bed fusion metal additive manufacturing, Mater. Des. 193 (2020).
[15] S. Chowdhury, N. Yadaiah, C. Prakash, S. Ramakrishna, S. Dixit, L.R. Gulta, D. Buddhi, Laser powder bed fusion: a state-of-the-art review of the technology, materials, properties & defects, and numerical modelling, J. Mater. Res Technol. 20 (2022) 2109–2172.
[16] D. Svetlizky, M. Das, B.L. Zheng, A.L. Vyatskikh, S. Bose, A. Bandyopadhyay, J. M. Schoenung, E.J. Lavernia, N. Eliaz, Directed energy deposition (DED) additive manufacturing: physical characteristics, defects, challenges and applications, Mater. Today 49 (2021) 271–295.
[17] A. Edwards, D. Weisz-Patrault, E. Charkaluk, Analysis and fast modelling of microstructures in duplex stainless steel formed by directed energy deposition additive manufacturing, Addit. Manuf. 61 (2023).
[18] L.C. Zhang, Y.J. Liu, S.J. Li, Y.L. Hao, Additive manufacturing of titanium alloys by electron beam melting: a review, Adv. Eng. Mater. 20 (5) (2018).
[19] A.A. Hemeda, C. Zhang, X.Y. Hu, D. Fukuda, D. Cote, I.M. Nault, A. Nardi, V. K. Champagne, Y. Ma, J.W. Palko, Particle-based simulation of cold spray: influence of oxide layer on impact process, Addit. Manuf. 37 (2021) 101517.
[20] K. Kang, J. Won, G. Bae, S. Ha, C. Lee, Interfacial bonding and microstructural evolution of Al in kinetic spraying, J. Mater. Sci. 47 (11) (2012) 4649–4659.
[21] R. Jenkins, B. Aldwell, S. Yin, S. Chandra, G. Morgan, R. Lupoi, Solid state additive manufacture of highly-reflective Al coatings using cold spray, Opt. Laser Technol. 115 (2019) 251–256.
[22] A.A. Hemeda, C. Zhang, X.Y. Hu, D. Fukuda, D. Cote, I.M. Nault, A. Nardi, V. K. Champagne, Y. Ma, J.W. Palko, Particle-based simulation of cold spray: Influence of oxide layer on impact process, Addit. Manuf. 37 (2021).
[23] A.W.Y. Tan, W. Sun, Y.P. Phang, M.H. Dai, I. Marinescu, Z.L. Dong, E.J. Liu, Effects of traverse scanning speed of spray nozzle on the microstructure and mechanical properties of cold-sprayed Ti6Al4V coatings, J. Therm. Spray. Techn 26 (7) (2017) 1484–1497.
[24] V.S. Bhattiprolu, K.W. Johnson, O.C. Ozdemir, G.A. Crawford, Influence of feedstock powder and cold spray processing parameters on microstructure and mechanical properties of Ti-6Al-4V cold spray depositions, Surf. Coat. Tech. 335 (2018) 1–12.
[25] R. Jenkins, B. Aldwell, S. Yin, S. Chandra, G. Morgan, R. Lupoi, Solid state additive manufacture of highly-reflective Al coatings using cold spray, Opt. Laser Technol. 115 (2019) 251–256.
[26] X. Chen, D. Inao, S. Tanaka, A. Mori, X.J. Li, K. Hokamoto, Explosive welding of Al alloys and high strength duplex stainless steel by controlling energetic conditions, J. Manuf. Process 58 (2020) 1318–1333.
[27] Q. Zhou, R. Liu, Q. Zhou, C. Ran, K.S. Fan, J. Xie, P.W. Chen, Effect of microstructure on mechanical properties of titanium-steel explosive welding interface, Mat. Sci. Eng. A-Struct. 830 (2022).
[28] M. Yang, H.H. Ma, Z.W. Shen, Z.C. Huang, Q.C. Tian, J. Tian, Dissimilar material welding of tantalum foil and Q235 steel plate using improved explosive welding technique, Mater. Des. 186 (2020).
[29] Q. Zhou, H.H. Lu, X.K. Lan, Y.S. Guo, K.Y. Liu, G.Y. Huang, B. Jia, P.W. Chen, Anisotropy in microstructure and shear properties of TA2/Q235 explosive welding interfaces, J. Mater. Res Technol. 25 (2023) 6472–6491.
[30] X. Wang, X.J. Wang, F. Li, J.X. Lu, H.X. Liu, Interface kinematics of laser impact welding of Ni and SS304 based on jet indentation mechanism, Met. Mater. Trans. A 51 (6) (2020) 2893–2904.
[31] H.M. Wang, A. Vivek, Y.L. Wang, G. Taber, G.S. Daehn, Laser impact welding application in joining aluminum to titanium, J. Laser Appl. 28 (3) (2016).
[32] H.M. Wang, D.J. Liu, J.C. Lippold, G.S. Daehn, Laser impact welding for joining similar and dissimilar metal combinations with various target configurations, J. Mater. Process Tech. 278 (2020).
[33] G. Gleason, S. Sunny, R. Mathews, A. Malik, Numerical investigation of the transient interfacial material behavior during laser impact welding, Scr. Mater. 208 (2022).
[34] S. Sunny, G. Gleason, R. Mathews, A. Malik, Simulation of laser impact welding for dissimilar additively manufactured foils considering influence of inhomogeneous microstructure, Mater. Des. 198 (2021).
[35] K. Davami, M. Vaseghi, N. Brooks, R. Rowe, N. Holtham, T. Southers, T. Um, L. Hackel, High-velocity laser accelerated deposition (HVLAD): an experimental study, Surf. Coat. Tech. 466 (2023).
[36] Y.L. Liao, S. Suslov, C. Ye, G.J. Cheng, The mechanisms of thermal engineered laser shock peening for enhanced fatigue performance, Acta Mater. 60 (13-14) (2012) 4997–5009.
[37] B. Mao, B. Li, D. Lin, Y.L. Liao, Enhanced room temperature stretch formability of AZ31B magnesium alloy sheet by laser shock peening, Mat. Sci. Eng. A-Struct. 756 (2019) 219–225.
[38] A. Siddaiah, B. Mao, Y.L. Liao, P.L. Menezes, Effect of laser shock peening on the wear-corrosion synergistic behavior of an AZ31B magnesium alloy, J. Tribol. -T Asme 142 (4) (2020).
[39] C.J. Yocom, X. Zhang, Y.L. Liao, Research and development status of laser peen forming: a review, Opt. Laser Technol. 108 (2018) 32–45.
[40] N.G. Shen, H.T. Ding, Q.H. Wang, H. Ding, Effect of confinement on surface modification for laser peen forming without protective coating, Surf. Coat. Tech. 289 (2016) 194–205.
[41] R.Y. Yang, Y.X. Hu, Plastic deformation mechanisms and their threshold pressures of Ti6Al4V thin-walled structures induced by laser peen forming, Opt. Laser Technol. 167 (2023).
[42] K. Ding, L. Ye, Laser Shock Peening: Performance and Process Simulation, Woodhead Publishing Ltd, Cambridge, 2009.

[43] R. Fabbro, J. Fournier, P. Ballard, D. Devaux, J. Virmont, Physical study of laser-produced plasma in confined geometry, J. Appl. Phys. 68 (2) (1990) 775–784.
[44] R. Fabbro, P. Peyre, L. Berthe, X. Scherpereel, Physics and applications of laser-shock processing, J. Laser Appl. 10 (6) (1998) 265–279.
[45] S.S. Harilal, M.S. Tillack, B. O'Shay, C.V. Bindhu, F. Najmabadi, Confinement and dynamics of laser-produced plasma expanding across a transverse magnetic field, Phys. Rev. E 69 (2) (2004).
[46] P. Peyre, A. Sollier, I. Chaieb, L. Berthe, E. Bartnicki, C. Braham, R. Fabbro, FEM simulation of residual stresses induced by laser Peening, Eur. Phys. J. - Appl. Phys. 23 (2) (2003) 83–88.
[47] X. Wang, F. Li, T. Huang, X.J. Wang, H.X. Liu, Experimental and numerical study on the laser shock welding of aluminum to stainless steel, Opt. Laser Eng. 115 (2019) 74–85.
[48] H. Gao, Y.W. Hu, Y. Xuan, J. Li, Y.L. Yang, R.V. Martinez, C.Y. Li, J. Luo, M.H. Qi, G.J. Cheng, Large-scale nanoshaping of ultrasmooth 3D crystalline metallic structures, Science 346 (6215) (2014) 1352–1356.
[49] J. Li, R.J. Zhang, H.Q. Jiang, G.J. Cheng, Scalable nano-patterning of graphenes using laser shock, Nanotechnology 22 (47) (2011).
[50] K. Edwards, S.P. Edwardson, C. Carey, C.J. Williams, G. Dearden, K. Watkins, Laser peen forming for 2D shaping and micro adjustment, ICALEO (2007) M605.
[51] S. Sadeh, A. Malik, Investigation into the effects of laser shock peening as a post treatment to laser impact welding, Mater. Des. 205 (2021).
[52] S. Sadeh, G.H. Gleason, M.I. Hatamleh, S.F. Sunny, H.L. Yu, A.S. Malik, D. Qian, Simulation and experimental comparison of laser impact welding with a plasma pressure model, Met. - Basel 9 (11) (2019).
[53] X. Wang, Y.X. Gu, T.B. Qiu, Y.J. Ma, D. Zhang, H.X. Liu, An experimental and numerical study of laser impact spot welding, Mater. Des. 65 (2015) 1143–1152.
[54] N. Kahraman, B. Gulenc, F. Findik, Corrosion and mechanical-microstructural aspects of dissimilar joints of Ti–6Al–4V and Al plates, Int. J. Impact Eng. 34 (8) (2007) 1423–1432.
[55] H. Huang, C. Yang, J.S. Tomblin, P. Harter, Stress and failure analyses of adhesive-bonded composite joints using ASTM D3165 specimens, J. Compos. Technol. Res. 24 (2) (2002) 345–356.
[56] M. Sokoluk, C.Z. Cao, S.H. Pan, X.C. Li, Nanoparticle-enabled phase control for arc welding of unweldable aluminum alloy 7075, Nat. Commun. 10 (2019).
[57] C.W. Visser, R. Pohl, C. Sun, G.W. Römer, B. Huis in 't Veld, D. Lohse, Toward 3D printing of pure metals by laser-induced forward transfer, Adv. Mater. 27 (27) (2015) 4087–4092.
[58] A. Kamyshny, J. Steinke, S. Magdassi, Metal-based inkjet inks for printed electronics, Open Appl. Phys. J. 4 (1) (2011).
[59] X. Wang, M. Shao, H. Jin, H. Tang, H.X. Liu, Laser impact welding of aluminum to brass, J. Mater. Process Tech. 269 (2019) 190–199.
[60] H.X. Liu, H. Jin, M. Shao, H. Tang, X. Wang, Investigation on interface morphology and mechanical properties of three-layer laser impact welding of Cu/Al/Cu, Met. Mater. Trans. A 50a (3) (2019) 1273–1282.
[61] P.M. Bellan, Fundamentals of Plasma Physics, Cambridge University Press, 2006.
[62] G.A.M.J.J. MacFarlane, R.R. Peterson, BUCKY-1-A 1-D Radiation Hydrodynamics Code for Simulating Inertial Confinement Fusion High Energy Density Plasmas, Wisconsin Fusion Technology Institute, 1995.
[63] Z.Y. Zhang, Q. Nian, C.C. Doumanidis, Y.L. Liao, First-principles modeling of laser-matter interaction and plasma dynamics in nanosecond pulsed laser shock processing, J. Appl. Phys. 123 (5) (2018).
[64] J. Xie, D. Nélias, H.W.L. Berre, K. Ogawa, Y. Ichikawa, Simulation of the cold spray particle deposition process, J. Tribol. -T Asme 137 (4) (2015).
[65] M. Alitavoli, A. Darvizeh, M. Moghaddam, P. Parghou, R. Rajabiehfard, Numerical modeling based on coupled Eulerian-Lagrangian approach and experimental investigation of water jet spot welding process, Thin Wall Struct. 127 (2018) 617–628.
[66] X. Song, K.L. Ng, J.M.K. Chea, W. Sun, A.W.Y. Tan, W. Zhai, F. Li, I. Marinescu, E. J. Liu, Coupled Eulerian-Lagrangian (CEL) simulation of multiple particle impact during Metal Cold Spray process for coating porosity prediction, Surf. Coat. Tech. 385 (2020).
[67] A. Fardan, C.C. Berndt, R. Ahmed, Numerical modelling of particle impact and residual stresses in cold sprayed coatings: a review, Surf. Coat. Tech. 409 (2021).
[68] G. Gleason, S. Sunny, S. Sadeh, H.L. Yu, A. Malik, Eulerian modeling of plasma-pressure driven laser impact weld processes, Namrc 48, 48th Sme North Am. Manuf. Res. Conf. 48 (2020) 204–214.
[69] W.Y. Li, C. Zhang, C.J. Li, H.L. Liao, Modeling aspects of high velocity impact of particles in cold spraying by explicit finite element analysis, J. Therm. Spray. Techn 18 (5-6) (2009) 921–933.
[70] W.Y. Li, K. Yang, S. Yin, X.P. Guo, Numerical analysis of cold spray particles impacting behavior by the eulerian method: a review, J. Therm. Spray. Techn 25 (8) (2016) 1441–1460.
[71] R.O. Davies, S. Parke, A generalization of gruneisens theory of solids and its application to solid argon, Philos. Mag. 4 (39) (1959) 341–358.
[72] X.Y. Wang, C.Z. Huang, B. Zou, H.L. Liu, H.T. Zhu, J. Wang, Dynamic behavior and a modified Johnson-Cook constitutive model of Inconel 718 at high strain rate and elevated temperature, Mat. Sci. Eng. a-Struct. 580 (2013) 385–390.
[73] Y.C. Lin, X.M. Chen, A combined Johnson-Cook and Zerilli-Armstrong model for hot compressed typical high-strength alloy steel, Comp. Mater. Sci. 49 (3) (2010) 628–633.